LES-based characterization of a suction and oscillatory blowing fluidic actuator

By J. Kim, P. Moin AND A. Seifert†

1. Motivation and objectives

Recently, a novel fluidic actuator using steady suction and oscillatory blowing was developed for active control of high-speed turbulent flows (Arwatz *et al.* 2008). The suction and oscillatory blowing (SaOB) actuator converts compressed air input into pulsed bi-stable oscillatory blowing at the actuator outlets. The mechanism for generating bi-stable oscillatory blowing is based upon the Coandă effect and use of a feedback tube. Also, actuator geometry was found to be crucial in producing robust control outputs (Arwatz *et al.* 2008). The SaOB actuator has been developed and tested for several canonical flow configurations as well as for external aerodynamic control problems (Wilson *et al.* 2013; Schatzman *et al.* 2014; Shtendel & Seifert 2014; Lubinsky & Seifert 2014, 2015; Schatzman *et al.* 2015). These recent studies showed that the addition of steady suction in close proximity to the pulsed blowing is important in increasing the efficacy and efficiency of this flow control approach.

The SaOB actuator is particularly interesting in two respects. First, generating oscillatory blowing does not involve any moving parts. Instead, a feedback tube is used to stably sustain the oscillation without additional external inputs. The length of the feedback tube is a key parameter determining oscillation frequency. Second, a suction system is employed to further increase total flow rates for a given inlet pressure. These two respects are based upon physical principles of fluid dynamics and are essential to efficiently and effectively producing oscillatory blowing.

The basic mechanisms of the SaOB actuator and some of the important flow features were examined experimentally (Arwatz *et al.* 2008; Wassermann *et al.* 2013). However, detailed characteristics of unsteady flows within the actuator are not completely understood. Geometric complexity, compressibility, and the strongly turbulent nature of the internal flows make diagnostics and characterization difficult.

An objective of this study is to predict the internal turbulent flows of the SaOB actuator and gain more understanding of the flow physics. A challenging part for prediction is to accurately resolve turbulent fluctuations as well as geometry of engineering complexity, both of which are important to correctly characterize the actuator. Large-eddy simulation (LES) based upon a novel unstructured-grid technique is applied to compute and characterize the internal flows within the SaOB actuator. The simulation tools are well validated for turbulent flows with multi-physics and tested to scale very well up to $O(10^6)$ cores. In addition to prediction, this study targets the development of reduced-order modeling techniques for fluidic oscillators, a process which is useful if not essential for integrated simulation of aerodynamic flow control system where actuator arrays are used on complex geometries with possible great variability of important scales.

† School of Mechanical Engineering, Tel Aviv University, Israel

2. Computational set-up

2.1. *Simulation domain*

Figures 1(a) and (b) show the computational domain in two different views. Throughout this paper, x is the streamwise direction, y is the spanwise direction, and z is the vertical direction. The full geometry of the SaOB actuator is used, and its complete geometric details are resolved. Downstream of the actuator outlets, a sufficiently large plenum is used so that oscillatory blowing through the actuator outlets does not interfere with the outflow boundaries. The flat surface from which the actuator injects momentum to the ambient air is inclined at 120° with respect to the $+x$ axis, similar with Wilson *et al.* (2013) Figure 1(a) also shows fifteen suction holes connected to an additional box modeling the ambient air. High-pressure air flows into a converging nozzle, as shown in Figure 1(c). The nozzle exit is at $x = 20$ mm, and its radius is $r_j = D_j/2 = 1.4$ mm. Upstream of the nozzle, there is an inlet tube larger in diameter than the nozzle. As shown in Figure 1(c), the cross-sectional area of the ejector contracts in the y direction, and the ejector exit is at $x = 58.5$ mm. The width of the ejector exit is 3.28 mm in the y direction. Inside the switching valve, a splitter leading-edge is at $x = 84.8$ mm, and the actuator outlets are at $x = 112$ mm. Both the ejector and the switching valve have the same height, 8.76 mm in the z direction. The feedback tube is modeled as an S-shaped channel underneath the actuator and links two feedback ports, as shown in Figure 1(c). The length of the feedback channel is 110 mm. As illustrated in Figure 1(c), 1 is used to denote a feedback port at $y < 0$ and 2 for a feedback port at $y > 0$. The same convention is used for the actuator outlets and the suction ports throughout this paper.

2.2. *Flow conditions*

The flow within the SaOB actuator is simulated at three different operating conditions. The actuator is placed in the still ambient air whose quantities are denoted by the subscript ∞. The actuator geometry is kept the same, and the inlet pressure is varied. At the nozzle inlet, total pressure p_0 and total temperature T_0 are specified. A gauge total pressure of $p_0 = 5$, 10, and 20 psig is used, corresponding to $p_0/p_\infty = 1.34$, 1.68, and 2.36, respectively. The total temperature at the nozzle inlet is kept the ambient. Solid wall boundaries are modeled as no-slip and adiabatic. On all the other boundaries, the ambient condition is used. These flow conditions result in the nozzle-exit Mach numbers (denoted by the subscript j) of $M_j = u_j/c_j = 0.68$, 0.95, and 1.27, respectively, where u_j is the nozzle-exit velocity and c_j the speed of sound at the nozzle exit. The Reynolds numbers based on the nozzle-exit conditions are $Re_j = \rho_j u_j D_j/\mu_j = 46000$, 67000, and 99000, respectively, where ρ_j denotes density and μ_j is molecular viscosity at the nozzle exit.

2.3. *Simulation conditions*

The high-fidelity, computational fluid dynamics code, CharLES†, is used to solve the fully compressible Navier–Stokes equations. The ideal gas is assumed with $\gamma = c_p/c_v = 1.4$, where c_p and c_v are the specific heats at a constant pressure and at a constant volume, respectively. The molecular viscosity is assumed to be a function of temperature only and to follow the power-law relation, $\mu/\mu_\infty = (T/T_\infty)^n$ where $n = 0.76$. The Prandtl number is assumed constant at $Pr = 0.7$. The subgrid-scale model of Vreman (2004) is used with a model constant $c = 0.07$ and a constant turbulent Prandtl number $Pr_t = 0.9$.

† http://www.cascadetechnologies.com/pdf/CHARLES.pdf

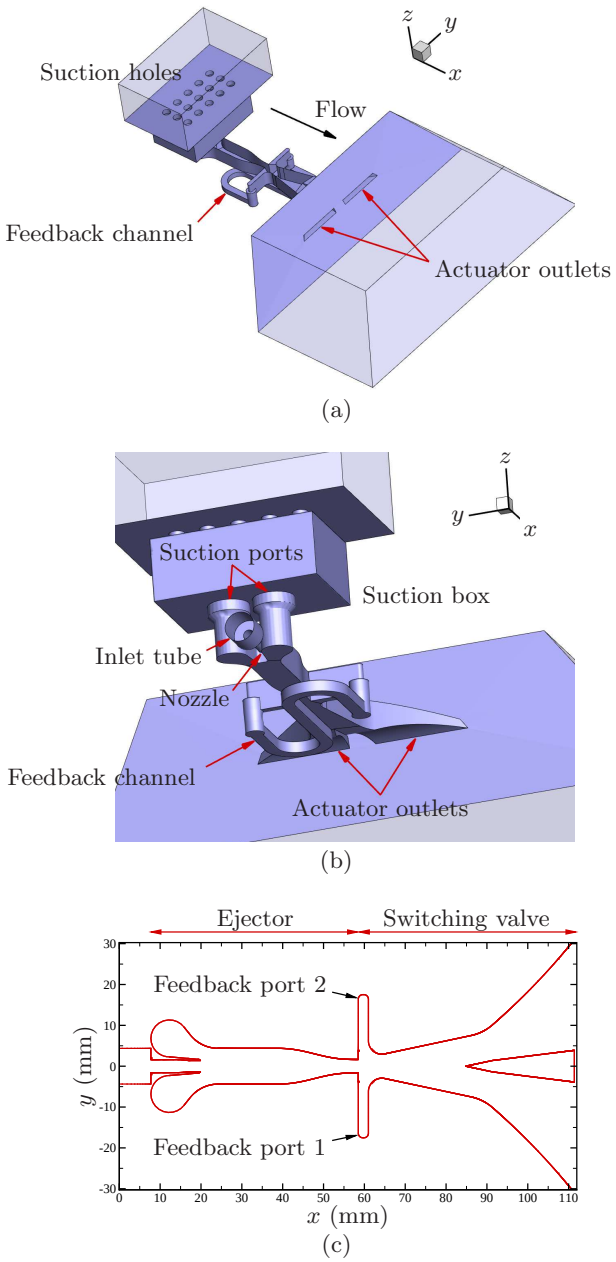

FIGURE 1. (a,b) Perspective view of the computational domain and (c) elevation view of the actuator boundaries on the $z = 0$ plane.

The governing equations are discretized in space using a cell-based finite volume formulation. The solutions are advanced in time using the standard third-order Runge–Kutta method at a constant time-step size of $\Delta t = 2.11 \times 10^{-8}$ s, which results in the maximum CFL number of approximately 1.0. The spatial discretization is non-dissipative and formally second-order accurate on arbitrary unstructured grids. In addition, the convective

fluxes are combined, depending on local grid quality (for example, element skewness), with fluxes computed by an HLLC-upwind discretization. Khalighi *et al.* (2011) provide more detailed discussion on the spatial discretization.

A base mesh of 2.2 million unstructured control volumes is generated and subsequently refined using ADAPT, the grid-adapting tool in the CHARLES suite of codes. The total number of control volumes for the adapted mesh is 47 million. For computational accuracy and efficiency, 99% of the total control volumes are hexahedral elements. A further refined grid simulation is performed using 280 million control volumes, which gives the same values for quantities of interest such as oscillation frequency, maximum outlet velocity.

Simulations are performed in the Argonne Mira cluster using 16,384 cores. There are approximately 2,848 control volumes per core, and the code scales well up to this number of cores. Wall-clock time for a single switching period is 11 hours for $p_0 = 5$ psig, 7 hours for 10 psig, and 5 hours for 20 psig.

3. Results

3.1. *Jet oscillation*

Flows are advanced in time until initial transients convect away from the computational domain and the jet in the switching valve establishes a bi-stable oscillation. The transient calculations are performed using the coarser base grid. The results are interpolated to the 47-million-cell grid and further time advanced to collect statistics. An oscillating state can be conveniently obtained by applying steady suction (or blowing) on one side of the switching-valve walls until the jet attaches, after which the wall is released back to a no-slip solid wall. This can quick achieve a self-sustained oscillation within the actuator.

Figure 2 shows instantaneous velocity contours for the inlet gauge pressure $p_0 = 5$ psig. Each figure is obtained at a different phase of the oscillation. The jet demonstrates an apparent switching between the two actuator outlets. The switching occurs at approximately the same frequency and continues without additional external inputs. Turbulent jet flows for $p_0 = 10$ psig and 20 psig also show similar switching, and thus their results are not shown here.

Oscillation frequency can be estimated by calculating mass flow rates near the feedback ports, as shown in Figures 3(a), (c), and (e). The mass flow rates are measured along $y = \pm 6.2$ mm within the feedback ports (see Figure 1(c)). These locations are chosen since they are less affected by strong turbulent fluctuations due to the oscillatory jet in the main flow passage. For each case, five oscillation periods are obtained. The mass flow rates can be modeled by a sinusoidal function with a constant period superimposed by high-frequency fluctuations. Oscillations within the two feedback ports are synchronous in time, consistent with the measurements (Arwatz *et al.* 2008). Note that the measured frequency in the experiments is not constant but fluctuates over the oscillation periods by about 10 Hz, due to strong turbulent fluctuations within the switching valve, as in the experiment.

The oscillation frequency can also be estimated using mass flow rates at the actuator outlets, as shown in Figures 3(b), (d), and (f). Again, a sinusoidal function with a constant period is used to estimate a switching frequency. Estimated frequencies are the same as those calculated at the feedback ports, showing that turbulent flows within the actuator oscillate at the same frequency. However, compared to measurement at the feedback ports, the mass flow rates at the actuator outlets are characterized by a rather slower

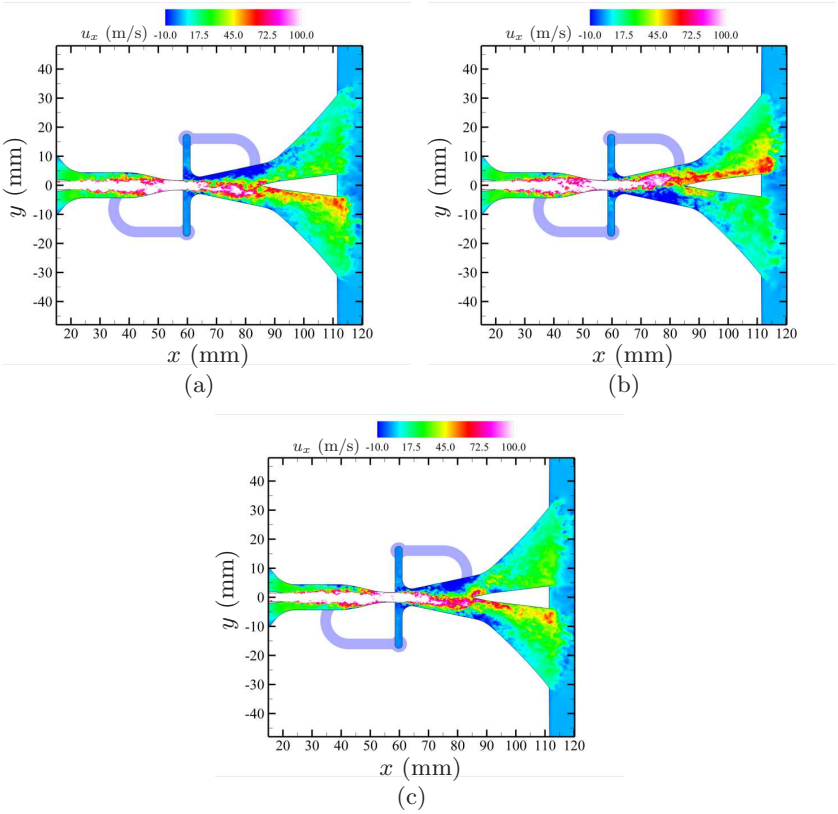

FIGURE 2. Instantaneous contours of streamwise velocity on the $z = 0$ plane at (a) $t = 57.58$ ms, (b) 60.96 ms, and (c) 64.34 ms. The contours are obtained for $p_0 = 5$ psig, where the oscillation period is 6.3 ms.

rise and rapid drop in time. Also, frequency modulation is larger, and higher-frequency fluctuations are stronger.

3.2. *Suction from the ambient air*

The SaOB actuator increases its total mass flow rates by utilizing additional mass flow rates from the ambient air (Arwatz *et al.* 2008). The additional air flow is generated by pressure gradients between the ambient air (outside of the suction holes) and the ejector, where a high-speed jet flow creates a low pressure zone (see Figures 1(a), (c)). This is useful in practice since lower inlet pressure is needed to produce the same flow rate at the actuator outlets as fluidic oscillators without any suction. Thus, power consumption of fluidic actuators can be reduced when they are integrated in aircraft control systems.

Figure 4 shows instantaneous streamwise velocity contours for $p_0 = 20$ psig. Also shown are instantaneous path-lines inside of the suction box, illustrating how the ambient air flows into the actuator.

Figures 5(a) through (c) show instantaneous mass flow rates at the two suction ports at three different inlet-pressure conditions. For all three cases, suction flow rates are approximately constant in time, and the two suction ports have nearly the same average flow rates. As inlet pressure increases, the average amount of suction increases and so do fluctuations amplitudes.

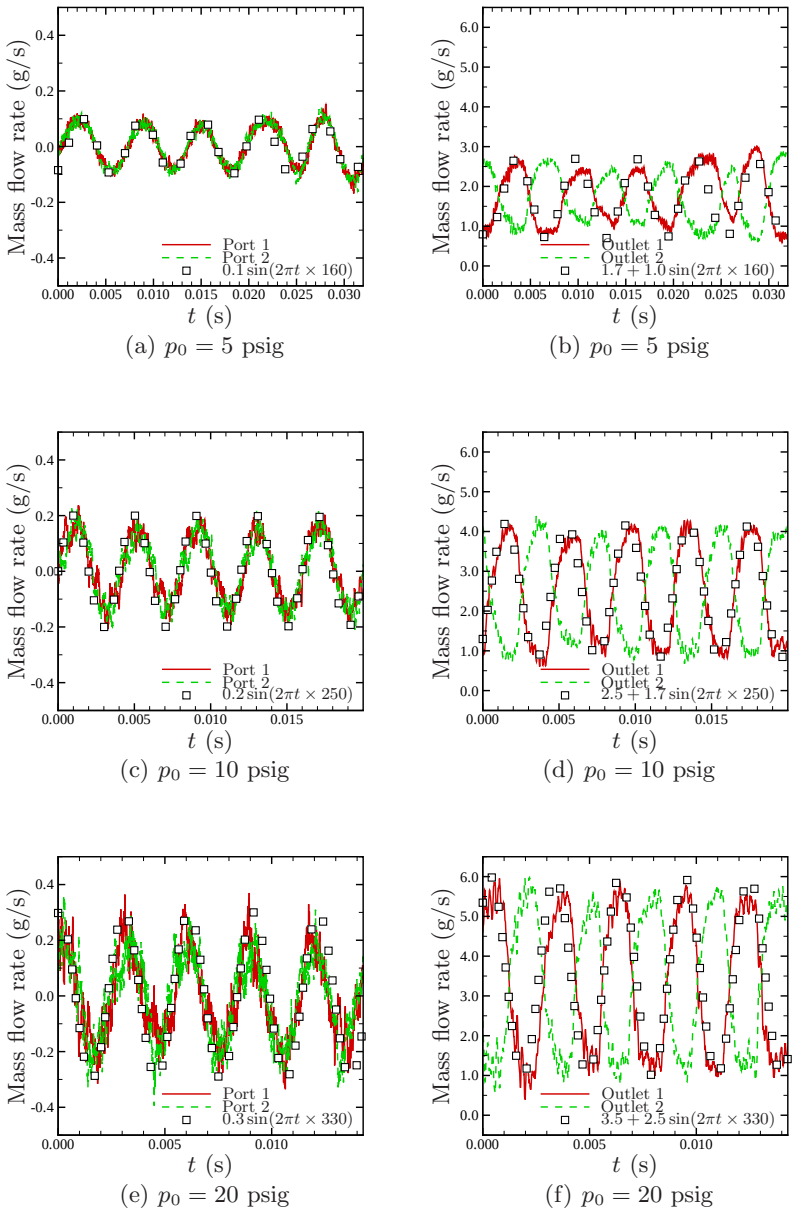

(a) $p_0 = 5$ psig (b) $p_0 = 5$ psig

(c) $p_0 = 10$ psig (d) $p_0 = 10$ psig

(e) $p_0 = 20$ psig (f) $p_0 = 20$ psig

FIGURE 3. Mass flow rates at the feedback ports (left column) and at the actuator outlets (right column).

The maximum velocities at the suction ports are 13 m/s, 18 m/s, and 23 m/s for $p_0 = 5$ psig, 10 psig, and 20 psig, respectively. The maximum suction velocities are obtained off the center of the suction ports. In previous studies, it was shown that the suction flow rate is maintained, as long as the number of open suction holes does not decrease significantly, creating larger suction velocities.

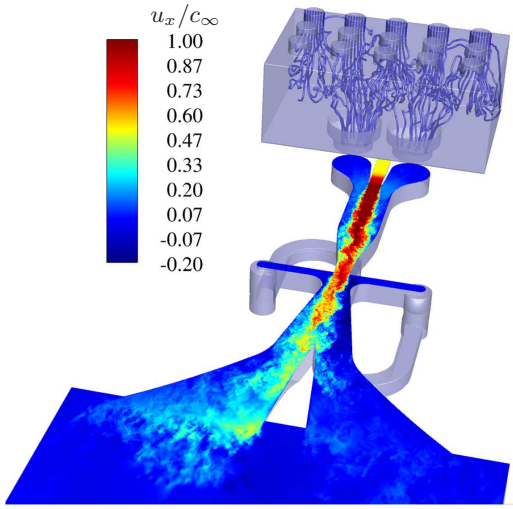

FIGURE 4. Instantaneous streamwise velocity contours on the $z = 0$ plane and instantaneous path-lines inside of the suction box. The simulation data are obtained for $p_0 = 20$ psig.

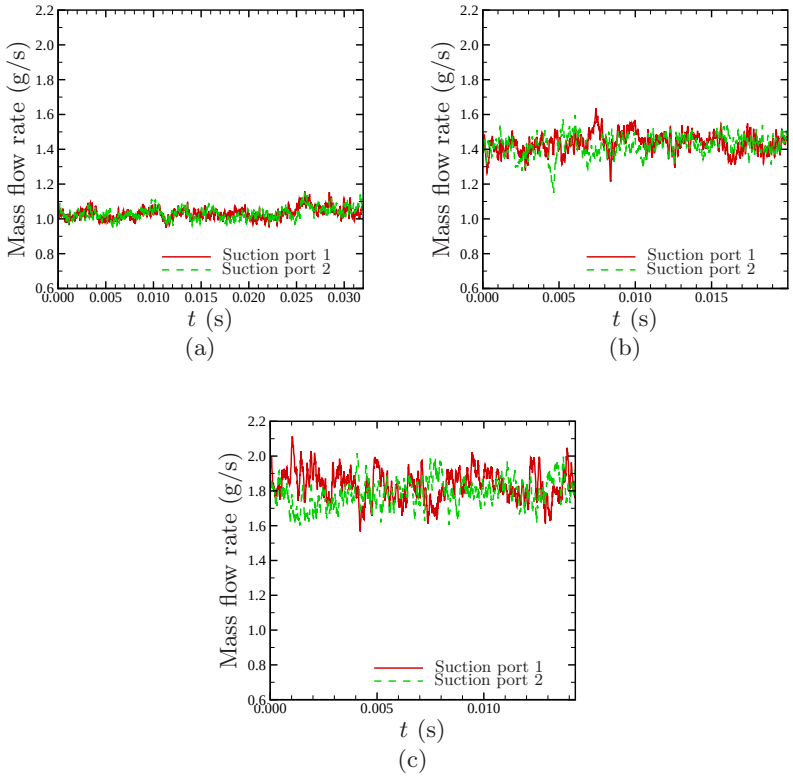

FIGURE 5. Time history of mass flow rates at the suction ports for (a) $p_0 = 5$ psig, (b) 10 psig, and (c) 20 psig.

TABLE 1. Mass flow rates measured for several components of the SaOB actuator.

	$p_0 = 5$ psig	10 psig	20 psig
Nozzle inlet (g/s)	1.51776	2.20197	3.17381
Actuator outlets (g/s)	3.54395	5.00943	6.73345
Suction ports (g/s)	2.06346	2.85633	3.62373
Feedback channel (g/s)	0.1	0.2	0.3

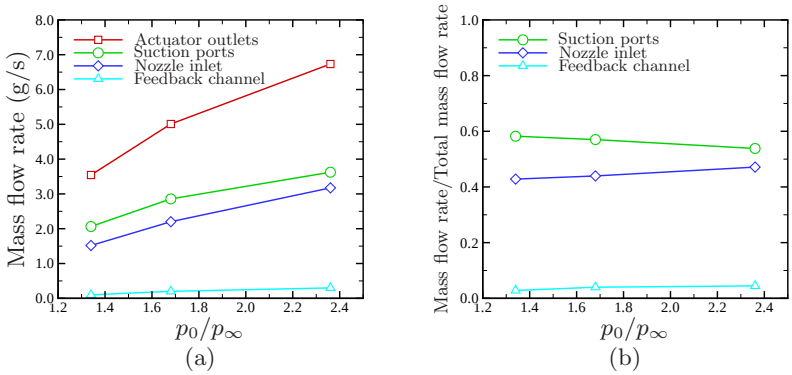

FIGURE 6. (a) Mass flow rates and (b) relative mass flow rates with respect to the total mass flow rates.

3.3. *Statistics*

Mass flow rates are computed at different locations of the actuator and tabulated in Table 1. As inlet pressure increases, all mass flow rates monotonically increase. Mass flow rates at the actuator outlets are the total mass flow rates. For the feedback channel, the maximum amplitudes of the fitted sinusoidal functions in Figures 3(a), (c), (e) are used, respectively. Note that the maximum mass flow rates within the feedback channel also increase with respect to the inlet pressure. Along with the observation that the oscillation frequency changes with the inlet pressure, this shows that the switching mechanism is not completely acoustic.

The mass flow rates are plotted with respect to p_0/p_∞ in Figure 6(a). Suction takes a significant portion of the total mass flow rates, followed by the nozzle. Figure 6(b) shows the relative mass flow rate with respect to the total mass flow rate. At the lowest pressure, suction from the ambient air takes nearly 60% of the total mass flow rate. As inlet pressure increases, the significance of suction gradually decreases, and the nozzle flow becomes more important. The maximum mass flow rates in the feedback channel are less than 4.5% of the total mass flow rates, although they do not contribute to net mass flow rates.

The solutions are time averaged for five oscillation periods. Figure 7(a) shows time-averaged streamwise velocity contours on the $z = 0$ plane. The inlet pressure is $p_0 = 5$ psig. The averaged flow field is symmetric with respect to $y = 0$, around which the jet oscillates. In Figure 7(b), the time-averaged streamwise velocity contour on the $y = 0$

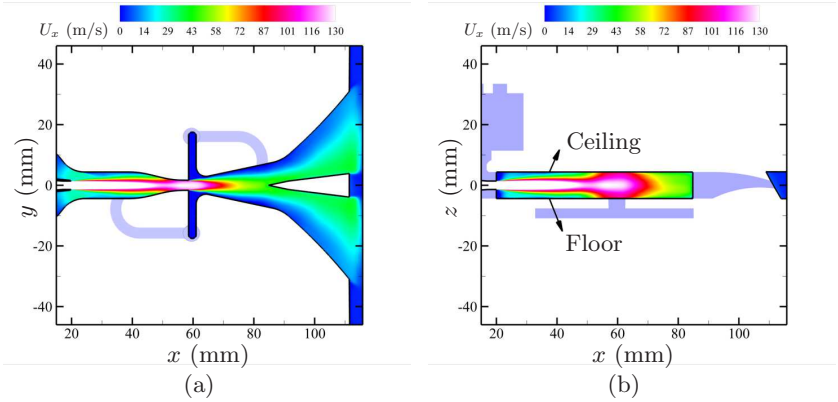

FIGURE 7. Time-averaged streamwise velocity contours on the (a) $z = 0$ and (b) $y = 0$ planes for $p_0 = 5$ psig.

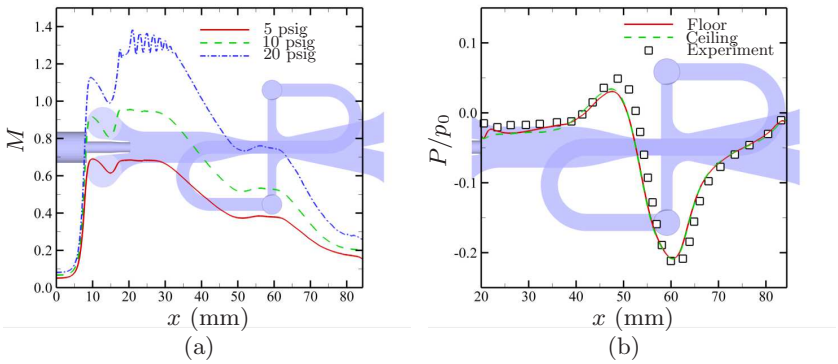

FIGURE 8. (a) Time-averaged Mach number along the actuator centerline ($y = 0$ and $z = 0$). (b) Relative gauge pressure along the centerline of the floor and ceiling of the actuator for $p_0 = 5$ psig.

plane is shown. Time-averaged flow fields at higher inlet-pressure conditions are qualitatively similar and not shown here.

Figure 8(a) shows time-averaged Mach number along the actuator centerline. At the nozzle exit, $M_j = 0.68$, 0.95, and 1.27 as inlet pressure increases, corresponding to 220 m/s, 287 m/s, and 340 m/s, respectively. The ejector-exit Mach number at $x = 58.5$ mm is 0.38, 0.53, and 0.75 for each inlet pressure. At the highest pressure $p_0 = 20$ psig, the nozzle exit becomes supersonic and shock-cell structures are observed. In Figure 8(b), time-averaged pressure along the streamwise direction is shown at the centerline of the actuator floor and ceiling. The floor and ceiling are defined in Figure 7(b). The maximum and minimum peak locations match the experiment as well as their amplitudes.

Figure 9 shows additional comparison with the experiment at $p_0 = 5$ psig. At the actuator outlets, the spanwise profiles of time-averaged velocity and fluctuating velocity rms in the streamwise direction are compared. Overall agreement is good in both quantites. Note that the measurement was made slightly downstream of the actuator outlets, while the LES data are obtained at the outlets.

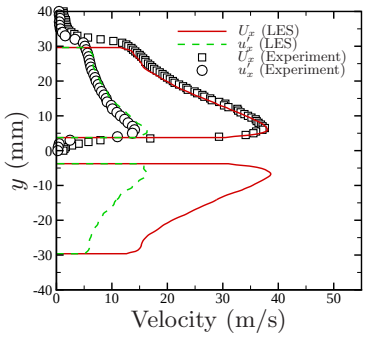

FIGURE 9. Comparison of streamwise velocity profiles at the actuator outlets for $p_0 = 5$ psig.

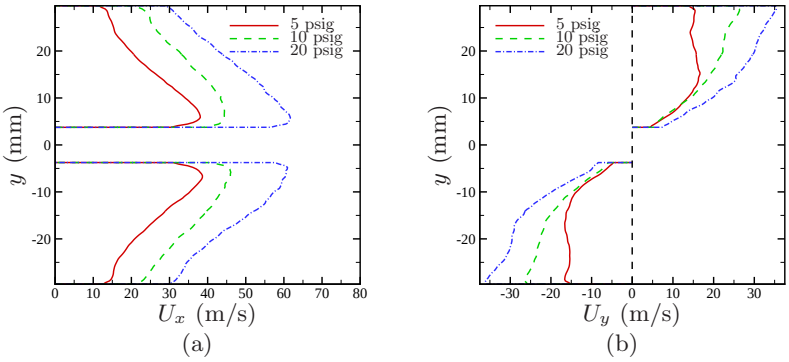

FIGURE 10. Time-averaged velocity profiles: (a) Streamwise and (b) spanwise components.

Figures 10(a) and (b) show time-averaged velocity components in each direction at the actuator outlets, measured at the centerline in the z direction. For all velocity components, there are substantial variations in the spanwise direction. Also, the spanwise velocities are 40 to 60% of the maximum streamwise velocities. The maximum velocity magnitudes are 41.8 m/s, 50.4 m/s, and 67.0 m/s for $p_0 = 5$ psig, 10 psig, and 20 psig, respectively.

An intrinsic feature of the SaOB actuator is a linear relation between the switching frequency and the maximum velocity that the actuator produces at the outlets. Figure 11 shows the experimental measurement at the actuator outlets and at the suction ports. When scaled with the spanwise width of the actuator outlets $h = 60$ mm, this linear relation gives a constant Strouhal number $fh/U_{\max} \approx 0.3$. This is one of the constraints that a reduced-order model for the SaOB actuator has to satisfy. The current simulations predict the relation reasonably well. The suction velocity at the center of the suction port is overpredicted by 3 to 6 m/s. Also shown is the LES result of Schatzman *et al.* (2015) who used an incompressible LES formulation. Comparison with the current data suggests that a fully compressible formulation is needed for higher inlet pressure.

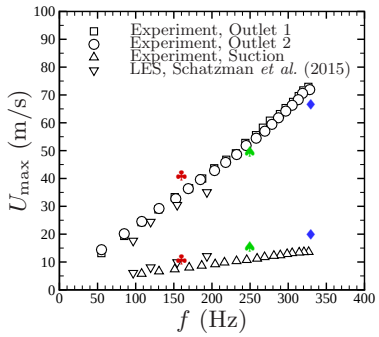

FIGURE 11. Relation between the switching frequency and the maximum velocity at the actuator outlets:; ♣, 5 psig; ♠, 10 psig; ♦, 20 psig; empty symbols, experiments.

4. Conclusions

The suction and oscillatory blowing (SaOB) actuator is designed for active flow control over a wide range of speeds, including high-speed turbulent flows. The actuator combines the concepts of steady suction and pulsed bi-stable oscillatory blowing into a compact active control device for higher control authority. The actuation is based upon a self-sustained mechanism of confined jet flows and does not require any moving parts. The actuator output is controlled primarily by pressure of a compressed air source and the geometric details, and no additional input is needed. The performance and mechanisms of the SaOB actuator have been studied previously by several research groups. While its basic mechanisms are investigated to some extent, detailed characteristics of internal turbulent flows are not well understood.

In this study, compressible turbulent jet flows within the SaOB actuator are investigated using large-eddy simulation (LES). The full actuator geometry is represented using an adapted unstructured grid with 47 million control volumes. Unstructured-grid LES enables complete geometric details to be described while keeping sufficiently high fidelity for accurate simulation of compressible turbulent flows.

Using LES, unsteady internal flows of the SaOB actuator are analyzed over a practical range of operating conditions. The oscillatory jet switching is well predicted for all three operating conditions, and the oscillation frequencies are in good agreement with the experiment. Also, LES correctly predicts a linear relation between oscillation frequency and maximum velocity at the actuator outlets. The actuator is characterized by parameters such as pressure ratio, maximum outlet velocity, oscillation frequency, suction to total flow rates. Detailed information on the unsteady actuator flows is reported to provide better understanding of the flow physics.

Based upon the LES-generated dataset, a study on reduced-order models for the actuator outputs is under way. While LES can predict turbulent flows within the actuator with sufficient accuracy, its computational cost is not negligible. LES for external aerodynamics, to which fluidic actuators are applied, is expensive at realistic flight conditions, even with wall modeling or hybrid RANS/LES techniques. Furthermore, external aerodynamics is controlled typically using many fluidic actuators. These imply that integrated simulation of aerodynamic control system is prohibitively expensive.

A viable solution is to model outputs from fluidic actuators analytically (or semi-analytically) and to apply the modeled actuation as a boundary condition to aerody-

namic control problems. Schatzman *et al.* (2015) used phase-averaged velocity profiles to analytically reconstruct actuator-outlet velocity profiles. In our ongoing study, dynamic mode decomposition (DMD) is employed since DMD is more suitable to extract lower-dimensional structures at well-defined frequencies. Preliminary DMD analysis shows that only a few dynamic modes are needed to capture important features of the actuator outputs.

Acknowledgments

This work is supported by the Boeing Company. Computing resources are provided by the Argonne National Laboratory through the ASCR Leadership Computing Challenge.

REFERENCES

Arwatz, G., Fono, I. & Seifert, A. 2008 Suction and oscillatory blowing actuator modeling and validation. *AIAA J.* **46** (5), 1107–1117.

Khalighi, Y., Nichols, J. W., Lele, S. K., Ham, F. & Moin, P. 2011 Unstructured large eddy simulation for prediction of noise issued from turbulent jets in various configurations. *AIAA Paper* 2011–2886.

Lubinsky, G. & Seifert, A. 2014 Flow control applied to the front rounded edge of a bluff body. *Int. J. Flow Control* **6** (1), 21–42.

Lubinsky, G. & Seifert, A. 2015 Flow control applied to the rounded front edges of a square prism. *Int. J. Flow Control* **7** (1-2), 1–18.

Schatzman, D., Wilson, J., Marom, L., Palei, V., Seifert, A. & Arad, E. 2015 Suction and oscillatory blowing interaction with boundary layers. AIAA SciTech (53rd AIAA Aerospace Sciences Meeting), Kissimmee, Florida, AIAA Paper No. 2015–0808.

Schatzman, D., Wilson, J. B., Arad, E., Seifert, A. & Shtendel, T. 2014 Drag-reduction mechanisms of suction-and-oscillatory-blowing flow control. *AIAA J.* **52** (11), 2491–2505.

Shtendel, T. & Seifert, A. 2014 Three-dimensional aspects of cylinder drag reduction by suction and oscillatory blowing. *Int. J. Heat Fluid Flow* **45**, 109–127.

Vreman, A. W. 2004 An eddy-viscosity subgrid-scale model for turbulent shear flow: Algebraic theory and applications. *Phys. Fluids* **16** (10), 3670–3681.

Wassermann, F., Hecker, D., Jung, B., Markl, M., Seifert, A. & Grundmann, S. 2013 Phase-locked 3D3C-MRV measurements in a bi-stable fluidic oscillator. *Exp. Fluids* **54** (3), 1–15.

Wilson, J. B., Schatzman, D., Arad, E., Seifert, A. & Shtendel, T. 2013 Suction and pulsed-blowing flow control applied to an axisymmetric body. *AIAA J.* **51** (10), 2432–2446.